ACS Catalysis
Research Article
pubs.acs.org/acscatalysis

In Situ Plasmonic Sensing of Platinum Model Catalyst Sintering on Different Oxide Supports and in O_2 and NO_2 Atmospheres with Different Concentrations

Pooya Tabib Zadeh Adibi,[†,§] Francesco Mazzotta,[†] Tomasz J. Antosiewicz,[†,∥] Magnus Skoglundh,[‡,§] Henrik Grönbeck,[†,§] and Christoph Langhammer*[,†]

[†]Department of Applied Physics, [‡]Applied Surface Chemistry and [§]Competence Centre for Catalysis, Chalmers University of Technology, SE-41296 Göteborg, Sweden
[∥]Centre of New Technologies, University of Warsaw, Banacha 2c, 02-097 Warsaw, Poland

Supporting Information

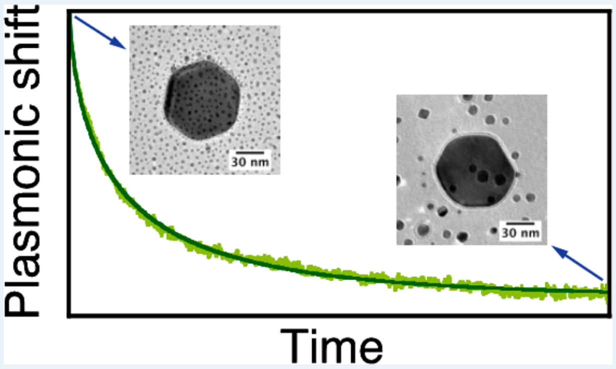

ABSTRACT: Improved understanding of thermal deactivation processes of supported nanoparticles via sintering is needed to increase the lifetime of catalysts. To monitor sintering processes under industrially relevant application conditions, in situ experimental methods compatible with elevated temperatures, high pressures, and harsh chemical environments are required. Here, we experimentally demonstrate the applicability of in situ indirect nanoplasmonic sensing (INPS) to investigate the sintering of Pt model catalysts on flat alumina and silica supports in O_2 and NO_2 atmospheres in real time and under operating conditions. Moreover, by means of finite-difference time-domain (FDTD) electrodynamics simulations, we establish a generic scaling approach to account for different inherent sensitivities of INPS sensor platforms featuring dielectric support layers with different refractive index. On the basis of these findings, we identify a universal, support-, and sintering-environment-independent correlation between INPS centroid shift signal and mean Pt particle size during the sintering process. As a first demonstration of the new possibilities offered by INPS and the obtained universal scaling to study sintering processes under different applied conditions, we investigate the dependence of the sintering rate of a SiO_2-supported Pt model catalyst on the O_2 concentration in Ar carrier gas. We find a clear dependence of the sintering rate on the O_2 concentration in the 0.05–0.5% O_2 concentration range.

KEYWORDS: *indirect nanoplasmonic sensing, sintering, nanoparticles, platinum, silicon dioxide, aluminum oxide, oxygen, nitrogen oxide*

INTRODUCTION

Heterogeneous catalysts are often realized as nanometer-sized metal particles dispersed on high-surface-area oxides, such as alumina or silica. However, because of the large surface-to-volume ratio of small metal particles, they are prone to sinter or coalesce into larger particles under operating conditions. This is a major cause of catalyst deactivation and leads to additional costs associated with either metal overloading or regeneration procedures.[1] Nanoparticle sintering is a complex physical and chemical phenomenon that is controlled by several parameters, such as particle size distribution, temperature, atmosphere, metal, and physicochemical properties of the support. Detailed understanding of the mechanisms and kinetics of sintering is therefore desirable to derive new strategies to limit the effect of these processes.

Despite extensive research during recent decades, the detailed mechanisms of sintering are far from fully understood.[2] The slow progress in this area is related to the fact that the phenomenon depends on various parameters, including metal–support interactions, support morphology, and gas environment.[3] Furthermore, there is the sheer complexity of the governing processes and a lack of suitable experimental methods that allow in situ scrutiny of sintering processes in real time and under relevant operating conditions. The latter is critical because it has been proven difficult to derive proper sintering mechanisms based on ex situ and post mortem analysis of particle size distributions (PSDs) alone.[2,4] An important step in this direction is the recent developments of in situ microscopy and spectroscopy in catalysis, as summarized in a recent review by Zhang et al.[5] Among such in situ techniques, environmental transmission electron microscopy (ETEM) has emerged as one of the most common and powerful methods to

Received: January 25, 2014
Revised: November 25, 2014
Published: December 1, 2014

investigate sintering processes, even though in most cases pressure limitations still apply.[6−14] In addition, regardless of the applied pressure, (E)TEM studies of sintering processes of nanoparticles have to be carried out with great care to avoid potential detrimental effects of the high-energy electron beam. Among spectroscopic methods, extended X-ray absorption fine structure (EXAFS) has been demonstrated as a promising tool to gain structural and chemical information on particles during sintering in harsh environment.[15−17] Nevertheless, EXAFS requires synchrotron light and often complex analysis.

In this work, we utilize in situ indirect nanoplasmonic sensing (INPS)[18] to monitor the sintering kinetics of Pt nanoparticle model catalysts on two different supports relevant in catalysis: namely, silica (SiO_2) and alumina (Al_2O_3). The sintering is studied at atmospheric pressure in Ar carrier gas with different O_2 and NO_2 partial pressures, which are environments that are known to promote particle growth.[7,8,19] The INPS measurements are complemented with ex situ TEM analysis to derive correlations between the plasmon signal and catalyst particle size. The present work represents a significant extension of experimental conditions used in our initial proof-of-principle study[19] and demonstrates that INPS is an efficient research tool for studies of sintering processes in operando. To illustrate the new possibilities offered by INPS and the obtained universal scaling to study sintering processes under different applied conditions on a relevant example, we investigate the O_2 concentration dependence of the sintering rate of a SiO_2-supported Pt model catalyst.

■ EXPERIMENTAL AND SIMULATION METHODS

Indirect Nanoplasmonic Sensing. The INPS technique is a versatile optical spectroscopy platform for materials science and catalysis applications.[18,20,21] It employs "sensor chips" that consist of gold nanoparticles fabricated on a glass substrate (see below) and covered by a thin layer of oxide material that mimics the support of a real catalyst. These sensor chips are (once the catalyst nanoparticles have been deposited on top) mounted in a comparably simple experimental setup (Insplorion X1 flow reactor system, Insplorion AB, Göteborg, Sweden) in which optical transmission/extinction through the nanofabricated "plasmonic" sensor chips is measured in real time.[19] The extinction spectra are recorded with a fiber-coupled fixed grating spectrometer (Avantes AvaSpec-1024). The spectral position of the plasmon peak is evaluated by tracking the centroid (i.e., the center of mass of the top part of the peak[22]) in real time using Insplorer software (Insplorion AB). In this way, real time sintering kinetic data can be obtained under realistic application/sintering conditions. Because low-power, near-visible light is used for illumination, INPS is noninvasive.

The INPS technology is based on the localized surface plasmon resonance (LSPR) phenomenon characteristic for (noble) metal nanoparticles. LSPR gives rise to strong absorption and scattering of near-visible light as well as significant enhancement of the local electric fields around the particle.[23] In a far-field extinction or transmission measurement, the LSPR manifests itself as a distinct peak at a specific wavelength, which strongly depends on the composition, size and shape of the metal particle, together with the dielectric environment.[24] The sensitivity toward local changes of the refractive index is the basis of nanoplasmonic sensing in general[25,26] and INPS in particular. In the present work, it is exploited to track the material rearrangements and consequent local nanoscale changes of the refractive index induced by the sintering process taking place on the INPS sensor surface. This is illustrated in Figure 1, which shows side-view schematic and corresponding TEM images of INPS arrangements with (panel a) as-deposited Pt particles, and of (panel b) Pt particles after sintering at elevated temperature. The images were obtained by fabricating the same structures as used on the "real" INPS chips onto TEM "windows" introduced in ref 27. Direct TEM analysis of the INPS chips is not possible because they are fabricated on 1-mm-thick glass supports. In this context, it is also relevant to briefly discuss the possibility of alloy formation between the Au disk sensor and the Pt catalyst nanoparticles. In this study and also in our previous one,[19] we find that the Pt volume on the sample is constant during the entire experiment; that is, no mass loss occurs (Figure S1). This indicates that the thin dielectric layers indeed completely block mass transport between the Pt and the Au. Moreover, if we had migration of Pt (or any optically "lossy" metal) to the gold disk, we would expect this to give rise to a spectral redshift of the LSPR and we observe the opposite.

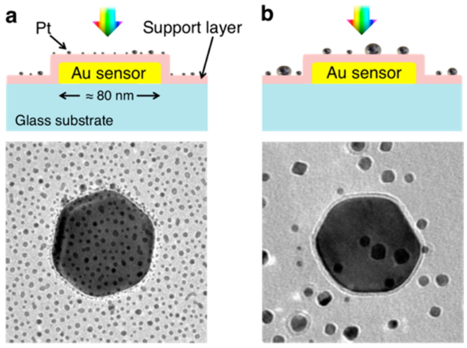

Figure 1. Schematic picture and corresponding TEM images (area 160 × 160 nm^2) of indirect nanoplasmonic sensing (INPS) platforms before and after sintering. (a) Schematic cross section of a gold sensor nanoparticle covered by a dielectric spacer layer comprising the INPS platform. Small Pt particles are grown on the dielectric spacer layer (i.e., the support). The corresponding TEM image shows the as-deposited Pt particles together with one INPS gold sensor particle that is covered with a 10-nm-thick SiO_2 layer. (b) Same as panel a, but after 12 h sintering treatment in O_2 at 600 °C, during which the Pt particles rearrange on the sensor chip, and hence, change the effective refractive index around the sensor particles.

Sample Fabrication. The INPS sensor chips consist of gold nanodisks with mean diameter of 80 nm and height of 20 nm. The discs are nanofabricated on fused silica substrates using hole−mask colloidal lithography.[28] Because the plasmon resonance frequency of the gold sensors is shape-dependent, sensor-related plasmon peak shifts during the high-temperature experiments have to be prevented. For this purpose, the sensor chips were heat-treated at 800 °C for 5 h to stabilize the gold particles prior to the deposition of the oxide support layer. During the heat treatment, the gold nanodisks become faceted and attain stable hexagonal shapes (Figure S2). After the annealing, the oxide support material is deposited, and the sensor is further stabilized by a second heat treatment for 36 h at 615 °C in air. In this study, the considered support materials are 10-nm-thick, plasma-enhanced chemical vapor deposition (PECVD) grown silica and RF-sputtered alumina. For sputtering and PECVD, FHR MS 150 and STS tools were used, respectively. As the final step, Pt nanoparticles with average size of ∼3.0 nm were grown on the two supports by means of thermal evaporation (deposition rate 0.05 nm/s) of an ultrathin granular Pt film with nominal thickness of 0.5 nm. For this purpose, an AVAC HVC600 electron-beam evaporator operated at a base pressure of 3×10^{-6} mbar was used.

Finite Difference Time Domain Simulations. The optical measurement of the sintering process was simulated using the finite difference time domain (FDTD) method. Figure 2a illustrates the employed simulation scheme which comprises a 25-nm-thick single gold disk with a bottom diameter of 60 nm and sidewall taper angle of 20 degrees. The substrate is a dielectric with $n = 1.45$. The disk and substrate are covered by a 10-nm-thick spacer layer with a refractive index set to either $n = 1.48$ (silica) or 1.62 (alumina). Platinum nanoparticles are modeled as spheres with a uniform diameter equal to the mean size (3 nm) and particle density (2.5×10^{-4} nm^{-2}) derived from TEM images of samples before exposure to sintering conditions. The Pt spheres are placed uniformly on an area 200 nm × 200 nm. The structure, both with and without Pt nanoparticles, is illuminated by a total field/scattered field source 300 nm × 300 nm in size. The scattered energy flow and power dissipation are monitored to calculate scattering, absorption, and extinction cross sections. To account for variability in Pt distribution, we performed five simulations with different Pt particle arrangement for each refractive index of the support layer for averaging. One simulation was performed for the case of a sample without Pt particles. The material properties are taken from the literature. Although the permittivity of small metal particles deviates from the corresponding bulk value,[29] we assume that this value is adequate enough to be used far away from the plasmon resonance. The current choice will underestimate losses.[30]

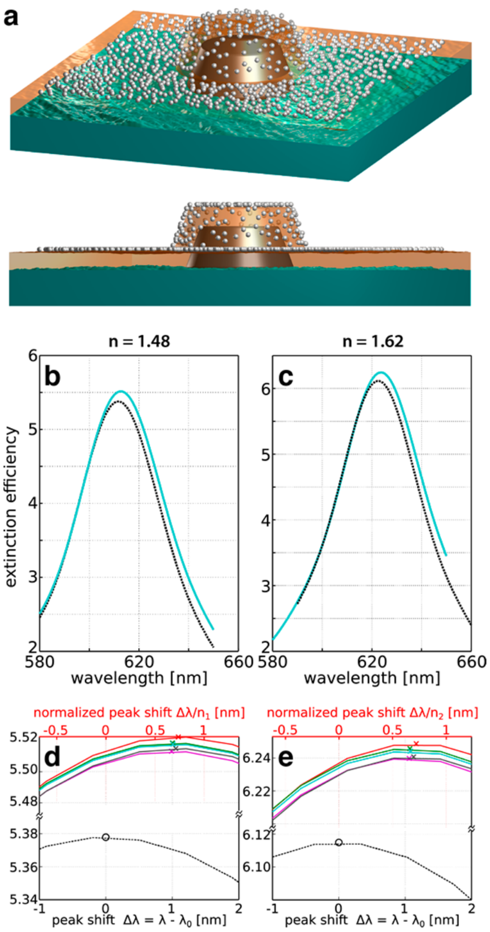

Figure 2. FDTD simulations to clarify the role of the refractive index of the support layer. (a) Schematic depiction of the simulated arrangement. Randomly distributed Pt spheres with diameter $D = 3$ nm decorate a gold sensor covered with a 10-nm-thick support layer. (b, c) Simulated extinction of a single Au nanodisk on a glass support, covered by a 10-nm-thick dielectric layer with refractive index $n = 1.48$ (silica) or $n = 1.62$ (alumina). The black dashed lines correspond to the LSPR response of a respective blank sensor. The green solid lines represent the response from sensors decorated with randomly distributed Pt spheres with diameter $D = 3$ nm and particle density corresponding to the experimental ones for equivalent average particle size. Clearly, in both cases, the presence of the Pt spheres induces a spectral red shift of the LSPR in the Au disk. The latter is larger for the support layer with the higher refractive index. (d, e) Zoom-in on the top part of the LSPR peaks for a blank sensor and a sensor covered with five different random arrangements of the Pt spheres at identical particle density. The bottom x-axis is arranged such that the peak shift is set to zero at the peak maximum for the blank sensor and shows again the larger red-shift of the LSPR peak upon Pt addition for the support layer with higher refractive index. The top (red) x-axis is scaled with the refractive index of the support and indicates that the support refractive index effect on the sensitivity of the INPS sensor efficiently can be canceled out by scaling.

Sintering Conditions. For sintering in O_2, the samples were heated to 600 °C in Ar, followed by a 10 min dwell to stabilize the temperature. After the temperature stabilization, the samples were exposed to 4% O_2 in Ar to initiate the sintering process. For the sintering experiments performed in NO_2, the temperature ramp in Ar was interrupted at 300 °C to expose the sample to 0.5% NO_2 for 15 min to stabilize the sensor chip in NO_2 atmosphere. We note that 300 °C is low enough that no sintering occurs during the stabilization procedure. Following this pretreatment, a second temperature ramp to 600 °C in Ar was applied. After stabilization at 600 °C, 0.1%, NO_2 was introduced to induce Pt nanoparticle sintering. After the designated sintering time, the samples were cooled in Ar to avoid further sintering. Complete temperature and gas flow rate diagrams for the sintering experiments both in O_2 and NO_2 are presented in Figure S3. We note that the used O_2 and NO_2 concentrations are representative for the conditions in oxidation catalysts for automotives, which motivates our choice.

For the sintering experiments in different O_2 concentrations, the samples were heated to 600 °C in Ar, followed by a 10 min dwell to stabilize the temperature. After the temperature stabilization, the samples were exposed to 0.05%, 0.1%, 0.2%, and 0.5% O_2, respectively, in Ar carrier gas at atmospheric pressure. The samples were kept in these conditions for 6 h, and subsequently were cooled in Ar.

TEM Imaging. The catalyst support material, silica or alumina, and subsequently Pt particles were deposited on silicon nitride TEM "windows"[27] and INPS chips simultaneously for maximal comparability. The TEM window samples were then placed alongside the INPS samples in the flow reactor and exposed to identical gas and temperature conditions. Bright-field TEM analysis was then performed post mortem using an FEI Tecnai G2 instrument at 200 kV acceleration voltage. The projected areas of the imaged Pt particles were approximated by circles and outlined by ImageJ software to obtain mean particle diameter and particle density on the surface. The contrast between the amorphous support and Pt particles arises mainly from the mass−thickness. The 40-nm-thick silicon nitride membrane (on which the support and Pt particles are deposited) adds notable weight to the background mass−thickness, which makes it harder to determine the size of small particles with reasonable precision because of inadequate contrast. Thus, to avoid errors in the estimation of very small particles, only those larger than 1 nm^2 (in projection) are counted in the analysis. Typical obtained particle size distributions (PSDs) are shown in Figure S4.

RESULTS AND DISCUSSION

Electrodynamics Simulations. To understand the role of the refractive index of the support for the measured signal, we performed FDTD electrodynamics simulations of the structures. Single gold disks on glass support, covered with a 10-nm-thick dilelectric layer with refractive index corresponding to either silica or alumina and monodispersed 3 nm Pt spheres were simulated. The configuration mimics the beginning of the sintering experiments (Figure 2a). Figure 2b and c shows the simulated extinction spectra corresponding to the LSPR response of a respective blank sensor (black dashed lines) and the response from sensors decorated with randomly distributed Pt spheres (green solid lines). For both support refractive indices, the presence of the Pt spheres induces a spectral red shift of the LSPR in the Au disk. The shift is larger for the support layer with the higher refractive index.

In Figure 2d and e, the top part of the LSPR peaks for a blank sensor and a sensor with Pt on top are magnified. The bottom *x*-axis is arranged so that the peak shift is set to zero at the peak maximum for the blank sensor and shows again the larger red-shift of the LSPR peak upon Pt addition for the support layer with higher refractive index. In addition, it is observed that the different local arrangement of the Pt particles around the sensor in the corresponding five simulations slightly affects the LSPR peak position. However, this effect is small and does not affect the general conclusions. To address the effect of the refractive index of the support layer, the top (red) *x*-axis in Figure 2d and e is scaled with the respective refractive index. Comparing the peak positions for the sensors decorated with Pt on the scaled peak shift axes reveals that they are identical after the scaling. This motivates the implementation of an identical scaling to the experimental data to account for the different sensitivities of INPS sensors featuring dielectric support materials with different refractive index.

Experimental Results. The results from sintering of Pt particles on silica or alumina support and upon exposure to either 4% O_2 (alumina and silica) or 0.1% NO_2 (silica) in Ar at 600 °C for 6 h are reported in Figure 3. Panels a−c show excerpts of the INPS-LSPR peaks for the considered systems at the beginning and end of the experiments. The discrete points correspond to the raw data from the spectrometer, and the solid lines, to the fitted polynomial functions used to determine the centroid readout signal. Clearly, a pronounced spectral blue shift is observed for all three systems during sintering. The LSPR peak positions (located between 570 and 580 nm) differ slightly from the simulation values in Figure 2b and c. The main reason is the strong dependence of LSPR peak positions on the shape of plasmonic particles. In the FDTD simulation a single gold disk is modeled, whereas in the experiments, the used heat-treated gold particles were rather hexagonal in shape. In addition, the lack of long-range order in the used Au nanoparticle arrays used in the experiment can shift the peak position to both the red and blue (compared with the simulated single disk), depending on the particle density in the array.[31,32] Importantly, however, the slight mismatch in peak position for either of these reasons will not affect the drawn conclusions.

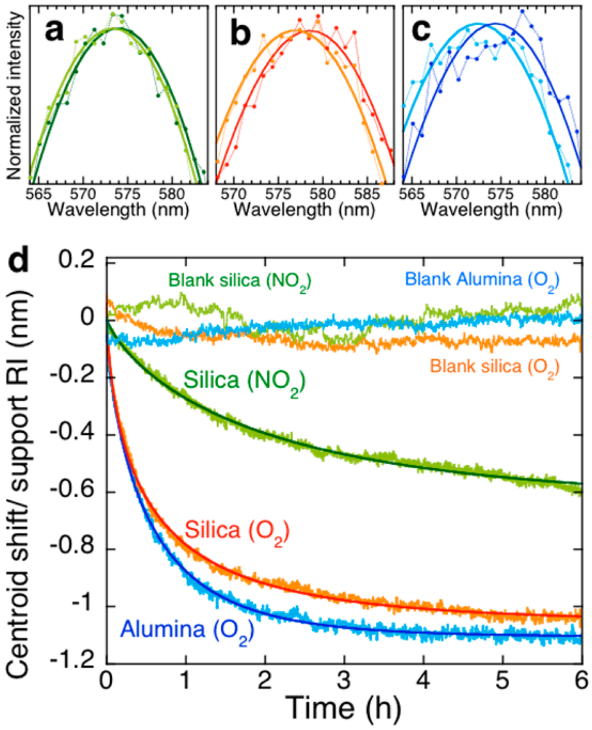

Figure 3. Excerpts of experimentally measured LSPR peaks measured at the beginning of the sintering experiment and after 6 h of sintering for (a) silica-supported Pt in 0.1% NO_2, (b) silica-supported Pt in 4% O_2, and (c) alumina-supported Pt in 4% O_2. The discrete points correspond to the raw data from the spectrometer, and the solid lines, to the fitted polynomial functions used to determine the centroid readout signal. Clearly, a pronounced spectral blue shift is seen for all three systems upon Pt particle sintering. (d) INPS sintering curves scaled with the refractive index of the support layer. The solid lines correspond to an exponential function fitted to the raw INPS curves. For all three systems, a distinct negative shift of the centroid signal (corresponding to a spectral blue-shift of the plasmon resonance) indicates significant sintering. The result for sintering of Pt particles supported on silica and alumina in 4% O_2 is very similar, and the curve shapes resemble each other (blue and orange curve). In contrast, the sintering process of silica-supported Pt in 0.1% NO_2 appears much slower and less severe. Corresponding INPS traces of blank sensors (i.e., no Pt) are also shown and exhibit a negligible centroid shift at the applied conditions.

Figure 3d shows the centroid shift measured with high temporal resolution. To account for the different sensitivities of the sensors due to the different refractive index of the support layer, the centroid signal is scaled with the support refractive index determined by ellipsometry (see Figure S5). The corresponding raw data without refractive index-scaling are shown in Figure S6. The INPS results for sintering of Pt particles on silica and alumina in 4% O_2 are similar, and the curve shapes resemble each other (blue and orange curve). In contrast, the sintering process of silica-supported Pt in 0.1% NO_2 appears to be much slower. Consequently, the refractive index-scaled centroid shift after 6 h of sintering in O_2 is almost double as compared with the corresponding shift for silica-supported Pt in 0.1% NO_2. This indicates a much more severe sintering in O_2 compared with NO_2 under the applied conditions. However, this is to be expected because of the lower NO_2 concentration. For reference, the signals from blank sensors without Pt exposed to the same conditions are also shown. Clearly, in contrast to the samples decorated with Pt nanoparticles, the signal is stable, that is, no centroid shift is observed in either O_2 or NO_2 atmosphere.

As the next step of our analysis, a series of ex situ TEM images was taken for the different samples after specific time intervals along the 6 h total sintering experiments followed by INPS. As an example, Figure 4 shows TEM images of Pt nanoparticles before gas exposure and during aging at 600 °C on (a–d) alumina in 4% O_2, (e–h) silica in 4% O_2 and (i–l) silica in 0.1% NO_2. In the bright-field TEM images, the Pt particles appear as dark features. The initial particle size is fairly similar for all three systems, with the particles on alumina being the smallest ones. Clearly, with time, the particle density decreases while an increase in average diameter, $\langle D \rangle$, and corresponding standard deviation are observed. This is in general agreement with the in situ INPS data shown in Figure 3d. Also in this data set, it is clear that the sintering kinetics in 0.1% NO_2 is much slower compared with 4% O_2. Analysis of the TEM images in terms of calculating particle volumes at different stages of the sintering further shows that the total Pt volume is conserved during the experiment, indicating that no Pt is lost to volatile PtO_x species (Figure S1). This is in good agreement with the study by Simonsen et al.,[7] which showed Pt mass conservation during sintgering in oxidizing atmosphere at 650 °C. Notably, their experiments were done on samples fabricated using the same evaporation system and the same amount of platinum as used in our study, which further strengthens the direct relevance of their results for our data.

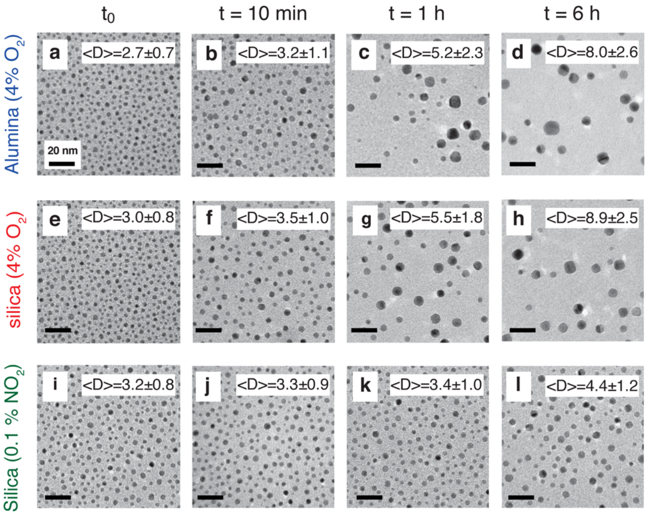

Figure 4. Time-sequence of TEM images of Pt nanoparticles supported on (a–d) alumina and sintered in 4% O_2, (e–h) supported on silica and sintered in 4% O_2, and (i–l) supported silica and sintered in 0.1% NO_2 at 600 °C. The scale bar in all images is 20 nm. A clear increase in average particle diameter, $\langle D \rangle$, and corresponding decrease in particle density is seen. Note specifically the very similar sintering behavior of Pt particles on alumina and silica in O_2, in contrast to the less severe sintering of Pt particles on silica in NO_2, in agreement with the scaled INPS centroid shift signal obtained in situ.

Using this intermittent TEM data, it is now possible to "translate" the scaled INPS signals into the average particle diameter to obtain in situ sintering kinetics with high temporal resolution by constructing specific "translation" curves. To do this, the scaled centroid shifts corresponding to the sintering time after which the different TEM images were recorded, are plotted versus the mean particle diameter (Figure 5a). We then fit a function of type $\Delta\lambda = A + B\langle D \rangle^{-n}$ to the discrete points as shown by Larsson et al.[19] In this way, empirical calibration functions for the different systems are obtained. The calibration functions can be used to translate the in situ INPS centroid signal to a high-resolution temporal evolution of the mean particle size during the sintering process. We obtain the following specific calibration functions for the three considered systems:

$$\Delta\lambda = -1.07 + 22.62\langle D \rangle^{-2.66} \qquad \text{silica } (NO_2)$$

$$\Delta\lambda = -1.21 + 10.34\langle D \rangle^{-2.17} \qquad \text{alumina } (O_2)$$

$$\Delta\lambda = -1.15 + 13.96\langle D \rangle^{-2.29} \qquad \text{silica } (O_2)$$

Interestingly, it becomes clear from comparing the obtained functions, as well as from visual inspection of Figure 5a, that the

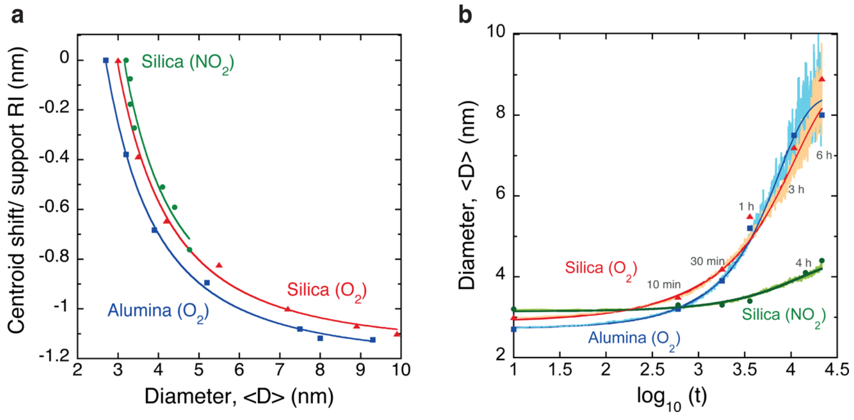

Figure 5. (a) Correlation between refractive index-scaled INPS centroid signal and mean particle diameter, $\langle D \rangle$ obtained from intermittent TEM data for sintered Pt particles on silica and alumina in 4% O_2 and 0.1% NO_2 atmosphere. The solid lines are obtained by fitting a function of the form $\Delta\lambda = A + B \langle D \rangle^{-n}$ to the experimental data points, as suggested by Larsson et al.[19] The latter yields an analytic expression that can be used to "translate" the INPS centroid signal to mean particle size, $\langle D \rangle$, to derive the sintering kinetics with high temporal resolution. We note the almost "universal" nature of the obtained calibrations, that is, their independence from both used support and applied gas environment. (b) High-resolution, real time experimental sintering kinetic data (solid lines) obtained by translating the centroid shift measured in situ during 6 h sintering experiments to mean particle size, $\langle D \rangle$, using the derived translation functions from the analysis in panel a. The dark solid lines correspond to fitted exponential functions to the raw data and serve as a guide to the eye. The discrete points show the mean particle diameter derived from TEM.

correlations between the scaled INPS signal and the mean particle diameter are very similar, and thus almost of “universal” nature. The only difference is basically the slightly different initial particle diameters in the three data sets.

This observation indicates two important findings: (i) the experimental approach is very robust and can, indeed, be applied when using different catalyst support materials and investigating sintering processes in different gas environments; (ii) it may eventually be possible, by collecting more data, to derive a truly universal calibration function linking the centroid shift signal with mean particle size, where the initial particle size before sintering is the only input required. However, this endeavor is beyond the scope of the present work because it would require significantly larger theoretical efforts to better understand the role of, for example, sintered particle shape and size distribution in the obtained INPS response.

In the next step, we use our calibration functions to convert the real time INPS centroid shift signals to mean particle diameter by the procedure described above. In this way, we obtain unique in situ sintering kinetic curves with unmatched temporal resolution that follow the rough trend given by the intermittently obtained TEM images over 6 h of sintering (Figure 5b). The INPS technique, however, reveals the sintering process at a much higher level of detail. At the same time, it is also important to generally note that a single parameter, such as the mean particle diameter, only to a certain approximation describes a PSD, and that relevant information about the sintering mechanism contained in the shape of the PSD may be lost. As a consequence, some caution must be taken when using a single parameter as the sole descriptor of sintering kinetics.

In the last part of this work, we apply the INPS technique together with the derived calibration function to investigate, for the first time to the best of our knowledge, the O_2 concentration dependence of Pt nanoparticle sintering on SiO_2 support. The experiments are conducted at 600 °C for 0.05, 0.1, 0.2, and 0.5% O_2 in Ar carrier gas at atmospheric pressure. Figure 6a shows the measured centroid shifts for the four different oxygen concentrations divided by the support refractive index. Clearly, smaller centroid shifts are observed for lower O_2 concentrations. By applying the derived calibration function for silica and O_2, we can now easily convert the centroid signal to a change in average particle diameter and thus conveniently obtain the temporal evolution of the mean particle diameter at the four different conditions (Figure 6b). It becomes very clear that the severity of sintering is strongly dependendent on the O_2 concentration in the gas stream. In 0.05% O_2, the particle size increases from 3 nm to ∼3.3 nm after 6 h, whereas in 0.5% O_2, the corresponding increase is to ∼4.9 nm. Similar to our observation, an enhanced sintering rate for higher oxygen partial pressure has been reported for Pt particles supported on alumina.[33,34] This result can be rationalized within the recently published theoretical framework of Ostwald ripening (the dominant sintering mechanism in our system as discussed in ref 8) by Ouyang et al., where it is predicted that different reactant partial pressures and, consequently, different oxygen coverages on the catalyst nanoparticles change their surface energy and thus their sintering behavior.[35]

To further analyze these data, in Figure 7, we plot the obtained mean particle size vs O_2 concentration after four different time intervals (1, 2, 3, and 6 h). We find a logarithmic dependence of the particle size on O_2 concentration at all stages, which indicates that the concentration dependence is expected to eventually saturate at even higher O_2 concentrations. This is in line with the argument that different oxygen surface coverage is responsible for the observed O_2 concentration dependence.

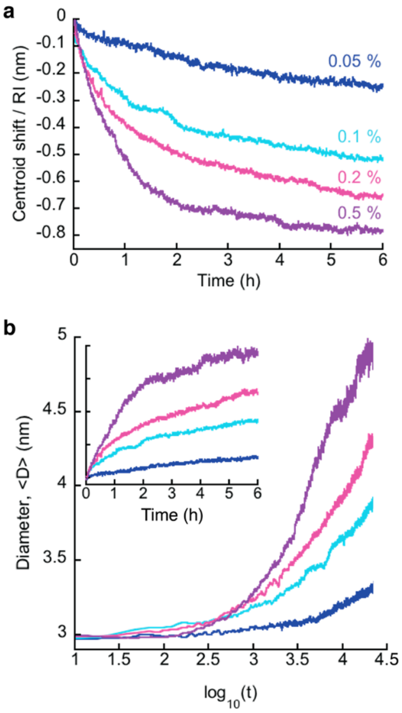

Figure 6. (a) Support refractive index-normalized INPS centroid shift signal from the sintering of a SiO_2-supported Pt model catalyst in four different O_2 concentrations in Ar at atmospheric pressure. Larger shifts are obtained at higher O_2 concentrations. (b) Corresponding temporal evolution of the mean particle size on a logarithmic and linear (inset) scale, as calculated from the measured INPS centroid shift by using the calibration function derived above. A strong O_2 concentration dependence of the sintering rate becomes apparent.

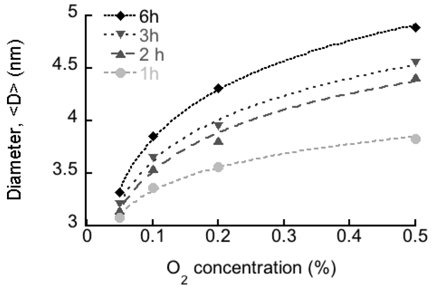

Figure 7. Correlation between mean particle size derived from the INPS measurement and the O_2 concentration in the gas stream after four different time intervals (the symbols correspond to 1, 2, 3, and 6 h). The dashed lines correspond to logarithmic fits to the experimental data points and show a weakening concentration dependence of the sintering rate for increasing O_2 concentration.

■ CONCLUSIONS

In summary, the presented INPS experimental platform shows significant potential as a robust and versatile experimental technique for in operando scrutiny of catalyst nanoparticle sintering. As the main result, we find gas environment- and support layer material-independent correlations between Pt particle size and the measured centroid shift response of the

INPS sensor during sintering by scaling the latter with the refractive index of the used support material. These correlations allow the derivation of high-resolution sintering kinetics in real time, which paves the way to use the INPS method for detailed in operando investigations of the role of (i) the catalyst support material, (ii) different gas environments, and (iii) other relevant issues such as initial size distributions and redispersion effects[36,37] in sintering processes. As a first demonstration of these new possibilities offered by INPS, we investigated the dependence of the sintering rate of a SiO_2-supported Pt model catalyst on the O_2 concentration in the Ar carrier gas. We find a strong dependence of the sintering rate on the O_2 concentration in the 0.05 to 0.5% range, which weakens for increasing O_2 partial pressure in the gas stream. These results are in line with recent theoretical predictions of the importance of adsorbate-modulated catalyst nanoparticle surface energies for the occurrence of catalyst sintering and redispersion.[35]

■ ASSOCIATED CONTENT

Ⓢ Supporting Information

The following file is available free of charge on the ACS Publications website at DOI: 10.1021/cs5015173.

Additional experimental information and data (PDF)

■ AUTHOR INFORMATION

Corresponding Author

*E-mail: clangham@chalmers.se.

Notes

The authors declare no competing financial interest.

■ ACKNOWLEDGMENTS

We acknowledge financial support from the Competence Centre for Catalysis, which is financially supported by Chalmers University of Technology, the Swedish Energy Agency, and the member companies: AB Volvo, ECAPS AB, Haldor Topsøe A/S, Scania CV AB, Volvo Car Corporation AB and Wärtsilä Finland Oy, the Swedish Research Council Project 2010-4041, the Chalmers Areas of Advance for Nanoscience and Nanotechnology and Transport, the Swedish Foundation for Strategic Research Framework Program RMA11-0037, the Polish National Science Center via the Project 2012/07/D/ST3/02152, the EMRP researcher Grant No. IND15-REG1, and the Knut and Alice Wallenberg Stiftelse for their support of the μ-fab cleanroom infrastructure in Sweden. The EMRP is jointly funded by the EMRP participating countries within EURAMET and the European Union.

■ REFERENCES

(1) Bartholomew, C. H. *Appl. Catal. A Gen.* **2001**, *212*, 17−60.

(2) Hansen, T. W.; Delariva, A. T.; Challa, S. R.; Datye, A. K. *Acc. Chem. Res.* **2013**, *46*, 1720−1730.

(3) Behafarid, F.; Roldan Cuenya, B. *Top. Catal.* **2013**, 1542−1559.

(4) Datye, A. K.; Xu, Q.; Kharas, K. C.; McCarty, J. M. *Catal. Today* **2006**, *111*, 59−67.

(5) Zhang, S.; Nguyen, L.; Zhu, Y.; Zhan, S.; Tsung, C.-K. F.; Tao, F. F. *Acc. Chem. Res.* **2013**, *46*, 1731−1739.

(6) Asoro, M. A.; Kovar, D.; Shao-Horn, Y.; Allard, L. F.; Ferreira, P. J. *Nanotechnology* **2010**, *21*, 025701.

(7) Simonsen, S. B.; Chorkendorff, I.; Dahl, S.; Skoglundh, M.; Sehested, J.; Helveg, S. *J. Am. Chem. Soc.* **2010**, *132*, 7968−7975.

(8) Simonsen, S. B.; Chorkendorff, I.; Dahl, S.; Skoglundh, M.; Sehested, J.; Helveg, S. *J. Catal.* **2011**, *281*, 147−155.

(9) Challa, S. R.; Delariva, A. T.; Hansen, T. W.; Helveg, S.; Sehested, J.; Hansen, P. L.; Garzon, F.; Datye, A. K. *J. Am. Chem. Soc.* **2011**, *133*, 20672−20675.

(10) Chang, S. L. Y.; Barnard, A. S.; Dwyer, C.; Hansen, T. W.; Wagner, J. B.; Dunin-Borkowski, R. E.; Weyland, M.; Konishi, H.; Xu, H. *J. Phys. Chem. Lett.* **2012**, *3*, 1106−1110.

(11) Benavidez, A. D.; Kovarik, L.; Genc, A.; Agrawal, N.; Larsson, E. M.; Hansen, T. W.; Karim, A. M.; Datye, A. K. *ACS Catal.* **2012**, 2349−2356.

(12) Yoshida, K.; Xudong, Z.; Bright, A. N.; Saitoh, K.; Tanaka, N. *Nanotechnology* **2013**, *24*, 065705.

(13) Creemer, J. F.; Helveg, S.; Hoveling, G. H.; Ullmann, S.; Molenbroek, a M.; Sarro, P. M.; Zandbergen, H. W. *Ultramicroscopy* **2008**, *108*, 993−998.

(14) de Jonge, N.; Bigelow, W. C.; Veith, G. M.; de Jonge, N. *Nano Lett.* **2010**, *10*, 1028−1031.

(15) Sanchez, S. I.; Menard, L. D.; Bram, A.; Kang, J. H.; Small, M. W.; Nuzzo, R. G.; Frenkel, A. I. *J. Am. Chem. Soc.* **2009**, *131*, 7040−7054.

(16) Roldan Cuenya, B.; Alcántara Ortigoza, M.; Ono, L.; Behafarid, F.; Mostafa, S.; Croy, J.; Paredis, K.; Shafai, G.; Rahman, T.; Li, L.; Zhang, Z.; Yang, J. *Phys. Rev. B* **2011**, *84*, 1−14.

(17) Matos, J.; Ono, L. K.; Behafarid, F.; Croy, J. R.; Mostafa, S.; DeLaRiva, a T.; Datye, a K.; Frenkel, a I.; Roldan Cuenya, B. *Phys. Chem. Chem. Phys.* **2012**, *14*, 11457−11467.

(18) Langhammer, C.; Larsson, E. M.; Kasemo, B.; Zorić, I. *Nano Lett.* **2010**, *10*, 3529−3538.

(19) Larsson, E. M.; Millet, J.; Gustafsson, S.; Skoglundh, M.; Zhdanov, V. P.; Langhammer, C. *ACS Catal.* **2012**, *2*, 238−245.

(20) Larsson, E. M.; Langhammer, C.; Zorić, I.; Kasemo, B. *Science* **2009**, *326*, 1091−1094.

(21) Langhammer, C.; Larsson, E. M. *ACS Catal.* **2012**, *2*, 2036−2045.

(22) Dahlin, A. B.; Tegenfeldt, J. O.; Hook, F. *Anal. Chem.* **2006**, *78*, 4416−4423.

(23) Bohren, C. F.; Huffman, D. R.; Clothiaux, E. E. *Absorption and Scattering of Light by Small Particles*; Wiley VCH Verlag GmbH: New York, 2010.

(24) Mayer, K. M.; Hafner, J. H. *Chem. Rev.* **2011**, *111*, 3828−3857.

(25) Anker, J. N.; Hall, W. P.; Lyandres, O.; Shah, N. C.; Zhao, J.; Van Duyne, R. P. *Nat. Mater.* **2008**, *7*, 442−453.

(26) Larsson, E. M.; Syrenova, S.; Langhammer, C. *Nanophotonics* **2012**, *1*, 249−266.

(27) Grant, A. W.; Hu, Q.; Kasemo, B. *Nanotechnology* **2004**, *15*, 1175−1181.

(28) Fredriksson, H.; Alaverdyan, Y.; Dmitriev, a.; Langhammer, C.; Sutherland, D. S.; Zäch, M.; Kasemo, B. *Adv. Mater.* **2007**, *19*, 4297−4302.

(29) Carmina Monreal, R.; Antosiewicz, T. J.; Peter Apell, S. *New J. Phys.* **2013**, *15*, 083044.

(30) Lermé, J.; Baida, H.; Bonnet, C.; Broyer, M.; Cottancin, E.; Crut, A.; Maioli, P.; Del Fatti, N.; Vallée, F.; Pellarin, M. *J. Phys. Chem. Lett.* **2010**, *1*, 2922−2928.

(31) Antosiewicz, T. J.; Apell, S. P.; Zäch, M.; Zorić, I.; Langhammer, C. *Phys. Rev. Lett.* **2012**, *109*, 247401.

(32) Antosiewicz, T. J.; Apell, S. P. *Opt. Express* **2014**, *22*, 2031−2042.

(33) Huang, F. H.; Li, C.-Y. *Scr. Metall.* **1973**, *7*, 1239−1243.

(34) Wynblatt, P.; Gjostein, N. A. *Prog. Solid State Chem.* **1975**, *9*, 21−58.

(35) Ouyang, R.; Liu, J.-X.; Li, W.-X. *J. Am. Chem. Soc.* **2013**, *135*, 1760−1771.

(36) Behafarid, F.; Pandey, S.; Diaz, R. E.; Stach, E. A.; Roldan Cuenya, B. *Phys. Chem. Chem. Phys.* **2014**, *16*, 18176−18184.

(37) Wettergren, K.; Schweinberger, F. F.; Deiana, D.; Ridge, C. J.; Crampton, A. S.; Rötzer, M.; Hansen, T. W.; Zhdanov, V. P.; Heiz, U.; Langhammer, C. *Nano Lett.* **2014**, *14*, 5803−5809.